Supplementary Information

Engineering of TMDC-OSC Hybrid Interfaces: The Thermodynamics of Unitary and Mixed Acene Monolayers on MoS_2

Stefan R. Kachel [a,†], *Pierre-Martin Dombrowski* [b,†], *Tobias Breuer* [b], *J. Michael Gottfried* [a], *Gregor Witte* [b,*]

[a] Fachbereich Chemie, Philipps-Universität Marburg, Hans-Meerwein-Straße 4, 35032 Marburg, Germany

[b] Fachbereich Physik, Philipps-Universität Marburg, Renthof 7, 35032 Marburg, Germany

*E-Mail: gregor.witte@physik.uni-marburg.de

†S.R.K. and P.-M.D. contributed equally to this work.

Contents

1. Details on the Monte Carlo simulations of TPD traces

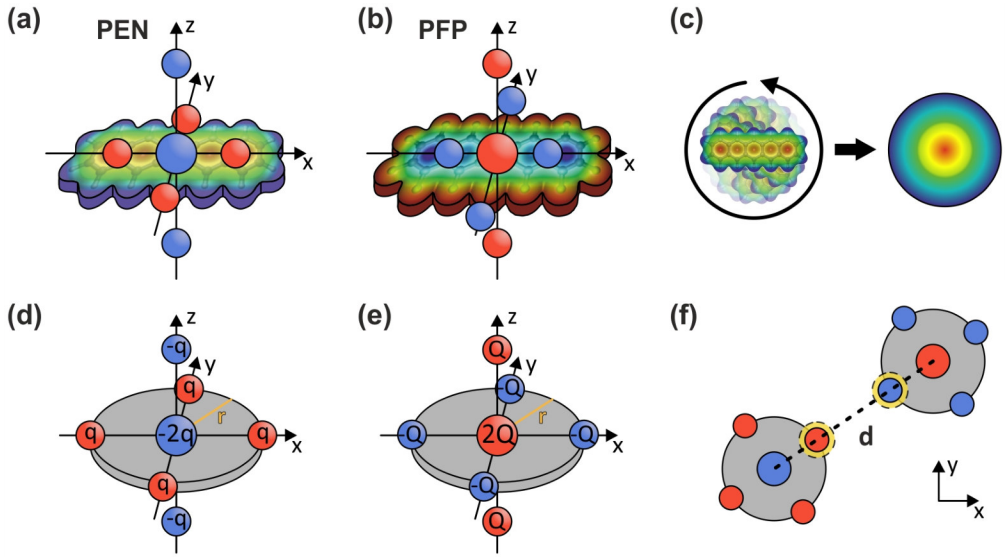

Figure S1: (a) and (b) Visualization of the quadrupole moments of PEN and PFP, respectively, as point charges (negative charges are blue, positive ones red) together with the molecular electrostatic potentials (MEPs). (c) Superposition of differently oriented PEN molecules with their MEPs. The average charge distribution is modeled as a circular disc with positive charges at the outer rim of the molecule and a negative charge at the center. (d) and (e) Illustration of the disc shaped models of PEN and PFP, respectively, with location of the point charges. (f) Illustration of the geometry for pair-wise intermolecular interactions. The yellow circles indicate the positions of H or F atoms for van der Waals interactions.

The Monte Carlo simulations of TPD traces presented in this work are based on a modified version of the algorithm described by Meng and Weinberg in Reference [S1]. Structural configurations of molecules within a unit surface (with periodic boundary conditions) are used to calculate interaction energies V_i for individual molecules. These interaction energies then effect desorption probabilities through the microscopic rate equation

$$r_i = \nu \exp\left(\frac{E_0 - V_i}{R\,T}\right). \qquad \text{(S1)}$$

Here, r_i is the rate of desorption of the molecule with index i, ν and E_0 are the prefactor and activation energy, respectively, for thermal desorption of a given molecular species in the limit of zero coverage, R is the gas constant and T is the surface temperature.

For intermolecular interactions, we consider only van der Waals (vdW) and electrostatic interactions. Due to the absence of Pauli repulsion and any significant interface dipole formed upon adsorption of the molecule on the MoS_2(0001) surface [S2, S3] we can neglect any substrate-mediated intermolecular interactions that would, for instance, be present on metallic surface. We have verified the absence of any notable interface dipole by measurements of the work functions of different molecular films of PEN and PFP on a MoS_2 crystal as well as the clean crystal surface, finding no significant differences (cf. Table S1).

The electrostatic interactions in our model are based on the molecular quadrupole moments of PEN and PFP that are the first non-zero terms in the multipole expansion of the electrostatic intermolecular interactions of PEN and PFP [S4]. In the far-field approximation, these quadrupole moments can be represented by seven point charges per molecule as illustrated in Figures S1 (a) and (b) for PEN and PFP, respectively. Since PEN and PFP are highly mobile on MoS_2 at (sub-) monolayer coverages, as evidenced by our experimental TPD data, molecules are not restricted to specific adsorption sites and relative orientations to the substrate, but can move freely across (and rotate freely on) the MoS_2 surface. Consequently, there is a multitude of relative orientations of molecules for pair-wise intermolecular interactions as illustrated in Figure S1 (c). We simplify our model by modeling molecules as two-dimensional circular discs, thus effectively averaging over all possible rotational orientations. The restriction to two dimensions is valid due to the flat-lying orientation of the molecules at (sub-) monolayer coverages that is retained even at elevated temperatures as evidenced by NEXAFS dichroism measurements (see Figure 1). Figures S1 (d) and (e) show the disc shaped models of PEN and PFP, respectively. We chose a disc radius of 5 Å that roughly reflects the molecular dimensions. This radius is equal for PEN and PFP to simplify heteromolecular structures.

The electrostatic potentials of PEN and PFP are modeled by seven point charges per molecule as illustrated in Figures S1 (d) and (e), so that the total charge adds to zero. Although the point charges only describe the molecular quadrupole moments accurately in the far-field approximation, we use this rather simple charge distribution to keep the model simple. Four equal charges are placed at the outer rim of the disc-shaped molecules. Using the quadrupole moments that were calculated in Reference [S4], one can calculate the average quadrupole moment in the molecular plane, $\theta_{\text{in plane}} = \frac{1}{2}(\theta_{xx} + \theta_{yy})$ (PEN: $4.45 \cdot 10^{-34}$ C cm^2; PFP: $-4.6 \cdot 10^{-34}$ C cm^2). Using the identity $\theta_{xx} = q_x\, x^2$ where x denotes the distance of the charge q_x from the center of the molecule, one can calculate an effective charge q in the

molecular plane. Since the two charges outside of the molecular plane on the z-axis have the same absolute value as those in the molecular plane, one can use q and θ_{zz} to calculate the distance of those charges from the molecular plane that is 7.1 Å for both PEN and PFP for a disc radius of 5 Å.

Because we want to neglect molecular orientation, interacting pairs of molecules are assumed to always have the same relative orientation with two charges of the outer rim of each molecule lying on the line connecting the centers of the two molecules, as illustrated in Figure S1 (f). This allows for a parameterization of the pair-wise interaction potential that only depends on the center-to-center distance d:

$$V(d) = \frac{q_1 q_2}{4\pi\varepsilon_0}\left(\frac{10}{d} - \frac{4}{d-r} - \frac{4}{d+r} + \frac{1}{d-2r} + \frac{1}{d+2r} - \frac{8}{\sqrt{d^2+r^2}} + \frac{8}{\sqrt{d^2+z^2}}\right.$$
$$+ \frac{4}{\sqrt{(d-r)^2+r^2}} - \frac{4}{\sqrt{(d-r)^2+z^2}} + \frac{4}{\sqrt{(d+r)^2+r^2}} - \frac{4}{\sqrt{(d+r)^2+z^2}}$$
$$\left. - \frac{8}{\sqrt{d^2+r^2+z^2}} + \frac{2}{\sqrt{d^2+4r^2}} + \frac{2}{\sqrt{d^2+4z^2}}\right) + V_{\mathrm{vdW}}(d)$$

Here, $r = 5$ Å is the disc radius and $z = 7.1$ Å is the distance of the two charges outside of the disc to the disc plane and V_{vdW} is the vdW potential. q_i denotes the charges at the outer rim of molecule i that is positive in the case of PEN and negative in the case of PFP.

The vdW potential is added to emulate the vdW box of a molecule. Therefore, we add a single hydrogen or fluorine atom to PEN or PFP, respectively, per molecule at the position of the charge that is closest to the interaction partner as illustrated by the orange circles in Figure S1 (f). We use the MM3 force field vdW potential [S5]

$$V_{\mathrm{vdW}}(d) = \sqrt{\varepsilon_1 \varepsilon_2}\left[184000\,\exp\left(-12\frac{d}{r_1+r_2}\right) - 2.25\left(\frac{r_1+r_2}{d}\right)^6\right]$$

where r_i are the vdW radii of the interacting species (hydrogen: 1.62 Å; fluorine: 1.71 Å) and ε_i are the respective energy parameters (hydrogen: 0.082 kJ mol^{-1}; fluorine: 0.31 kJ mol^{-1}) [S6].

Due to the relatively large size of the two molecular species studied in this work, PEN and PFP, discrete adsorption sites are not as clearly defined as in the case of small adsorbates such as CO. Moreover, at the elevated temperatures that occur in our TPD experiments, molecules can

be assumed to be able to move freely on a chemically inert substrate such as MoS_2, which is corroborated by our experimental TPD data and our STM data. Therefore, we model the MoS_2 surface as a jellium-like system with a uniform binding energy that does not favor specific adsorption sites. Between desorption events, molecules are allowed to diffuse freely until the mean square displacement of all molecules, $\langle \Delta x^2 \rangle$, reaches $\langle \Delta x^2 \rangle = (a\,\overline{D})^2$ where $\overline{D}$ is the nearest-neighbor distance in a uniformly spaced layer at the current surface coverage and a is a scaling factor. Thus, the mean diffusion length scales with surface coverage. We chose $a = 6$ as no notable changes to the simulated TPD traces were observed for larger values of a.

The procedure of the algorithm can be summarized as follows:

(1) Populate a rectangular unit surface with N molecules in a uniformly spaced structure for the given initial surface coverage. Assign Maxwell-Boltzmann distributed random velocities according to the initial surface temperature.
(2) Calculate molecular diffusion while monitoring the mean square displacement $\langle \Delta x^2 \rangle$ of all molecules. Stop diffusion when $\langle \Delta x^2 \rangle = (a\,\overline{D})^2$.
(3) Use equation S1 to calculate the individual desorption rates r_i for all molecules for the given spatial distribution of molecules.
(4) Randomly chose a molecule of index k that is allowed to desorb with a probability $p_k = {}^{r_k}/_{r_{\max}}$ where $r_{\max}$ is the current largest desorption rate of all molecules. Repeat until one molecule desorbs successfully.
(5) Remove the desorbed molecule and increase time by $\tau = (\sum_i r_i)^{-1}$, temperature by $\beta\tau$ and kinetic energy by $k_B\beta\tau$.
(6) Repeat steps (2) – (5) until all molecules have desorbed.

For the initial velocity distribution, we chose a 2D Maxwell-Boltzmann distribution. To account for the coverage-dependent mean free path of the molecules, we chose a first-order approximation and scale the Maxwell-Boltzmann velocities with $(1 - \theta)$ where θ is the surface coverage. Thus, we assign no velocity at maximum coverage and the Maxwell-Boltzmann distribution in the zero-coverage limit.

Periodic boundary conditions are implemented by replicating the rectangular unit surface to create eight identical surrounding unit surfaces. Intermolecular forces and interaction energies are calculated under consideration of these identical neighboring unit surfaces. Inclusion of

more neighboring unit surfaces does not change the simulated TPD traces due to the limited range of the intermolecular interactions.

As activation energies and prefactors, we chose the experimental results for the smallest initial coverages. These values are then fine-tuned manually to fit low-coverage simulated TPD traces to the experimental ones. Then, the interaction parameters, i.e., the charges of PEN and PFP, are adjusted so that the larger-coverage TPD traces match the experimentally recorded coverage series.

For heterostructures of PEN and PFP, we assume no structural order with regard to the intermixture. Instead, the species is randomly assigned to each individual molecule with equal probabilities for PEN and PFP, creating a randomized intermixture with an average stoichiometric ratio of 1:1 PEN:PFP. Due to the attraction between PEN and PFP, these randomized distributions tend to form ordered structures of alternating species once the coverage is sufficiently small to allow for structural reconfigurations.

The TPD traces presented in this work are averaged from at least 50 individual computations with randomized starting conditions. For homomolecular films, 64 molecules are used per run. Since in heteromolecular films, two TPD traces are simultaneously created from a single ensemble of molecules, we use 100 molecules for mixed films. Because time / temperature steps vary between these individual runs, TPD traces were averaged over temperature bins of equal size. For homomolecular films, we chose a bin size of 0.1 K. For heteromolecular films, we chose a larger bin size of 0.5 K due to a larger run-to-run variation of the TPD traces caused by the randomization of the stoichiometric ratio and spatial distribution of PEN and PFP in mixed films.

2. Work functions of molecular films on MoS_2

Table S1: Work functions of clean MoS_2, monolayers (nominal thickness: 3 Å) of PEN and PFP on MoS_2, multilayers of PEN and PFP on MoS_2 and a multilayer heterostack of PEN and PFP on MoS_2.

Sample	Work Function [eV]
MoS_2	4.62
MoS_2 + 3 Å PFP	4.59
MoS_2 + 3 Å PEN	4.63
MoS_2 + 20 Å PFP	4.59
MoS_2 + 20 Å PEN	4.58
MoS_2 + 20 Å PFP + 20 Å PEN	4.58

To verify that no interface dipole is formed upon adsorption of PEN and PFP on MoS_2, we have measured the work functions of clean MoS_2, monolayers (nominal thickness: 3 Å) of PEN and PFP on MoS_2, multilayers of PEN and PFP on MoS_2 and a multilayer heterostack of PEN and PFP on MoS_2 by means of the Kelvin probe technique at room temperature. The results are shown in Table S1. As a standard reference, we have used clean Au(111) surfaces with a work function of 5.35 eV [S7]. Repeated measurements on the same sample yield a relative accuracy of 0.02 eV. The absolute values are subject to additional uncertainties due to the referencing process via Au(111).

Considering the relative accuracy of the Kelvin probe measurements, no significant change of the work function of MoS_2 upon deposition of molecular films is found. The absolute value of the work function of bulk MoS_2 lies within the range of reported results from ultraviolet photoelectron spectroscopy of 4.542 eV to 4.75 eV [S8-S10].

3. Leading-edge analysis of multilayer TPD traces

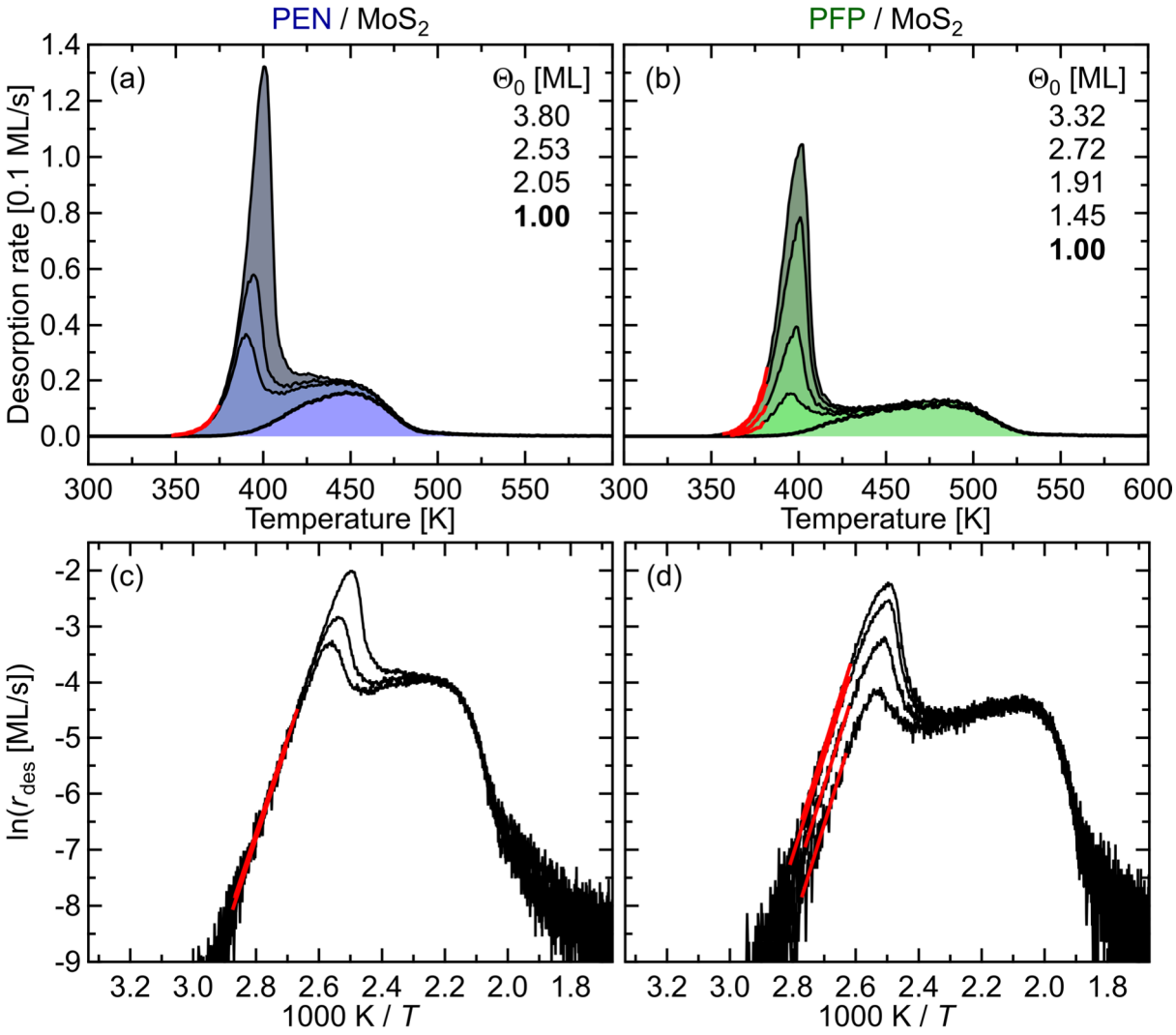

Figure S2: (a) and (b) Series of multilayer TPD traces for different film thicknesses of PEN and PFP, respectively, on MoS_2. Four point-reduction (four measured data points are averaged) for better visualization. Film thicknesses range from 3 Å to 12 Å. The nominal monolayers are marked with bold lines. The section of the leading edge that was used for the leading-edge analysis is indicated by bold, red traces. All measurements were performed with heating rates of 1 K/s by mass spectrometric detection of m/z = 278 amu for PEN and m/z = 530 amu for PFP. (c) and (d) Leading-edge analysis for PEN and PFP on MoS_2, respectively. TPD traces without point-reduction used for the analysis. The linear fit is marked as a bold, red line. The fitting results are given in Table S2.

Leading-edge analysis (LEA), according to:

$$\ln(r) = -\frac{E_\mathrm{d}}{RT} + \ln(\nu) \qquad \text{(S2)}$$

Table S2: Fitting results ($y = a + bx$) as well as desorption energies and prefactors for the LEA of PEN and PFP on MoS_2 as shown in Figure S2.

Coverage [ML]	a	b [K]	E_d [kJ/mol]	ν [s^{-1}]
PEN				
2.05	40.9±1.2	-17030±424	141.6±3.5	$10^{17.8\pm0.5}$
2.53	40.6±1.0	-16883±373	140.4±3.1	$10^{17.6\pm0.5}$
3.80	40.6±0.7	-16899±261	140.5±2.2	$10^{17.6\pm0.3}$
PFP				
1.45	42.3±1.8	-18095±673	150.4±5.6	$10^{18.4\pm0.8}$
1.91	42.3±1.0	-17836±364	148.3±3.0	$10^{18.4\pm0.4}$
2.72	42.6±0.6	-17757±231	147.6±1.9	$10^{18.5\pm0.3}$
3.32	43.3±0.5	-17950±192	149.2±1.6	$10^{18.8\pm0.2}$

4. Modified leading-edge analysis of monolayer

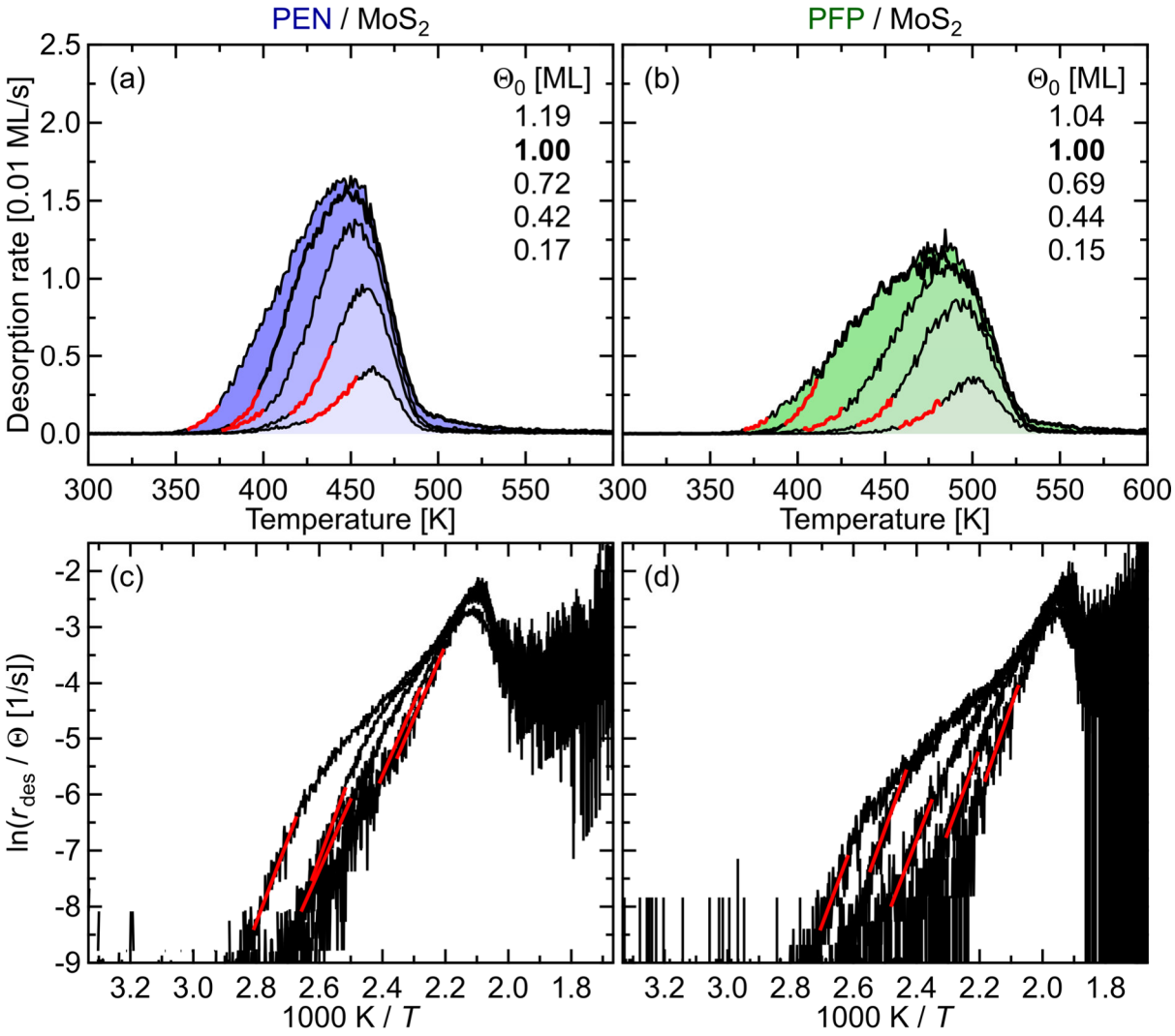

Figure S3: (a) and (b) Series of (sub-) monolayer TPD traces for different film thicknesses of PEN and PFP, respectively, on MoS_2. Four point-reduction (four measured data points are averaged) for better visualization. Film thicknesses range from 0.5 Å to 3 Å. The nominal monolayers are marked with bold lines. The section of the leading edge that was used for the modified leading-edge analysis is indicated by bold, red traces. All measurements were performed with heating rates of 1 K/s by mass spectrometric detection of m/z = 278 amu for PEN and m/z = 530 amu for PFP. (c) and (d) Modified leading-edge analysis for PEN and PFP on MoS_2, respectively. TPD traces without point-reduction used for the analysis. The linear fit is marked as a bold, red line. The fitting results are given in Table S3.

Modified leading-edge analysis (mLEA), according to:

$$\ln\left(\frac{r}{\theta}\right) = -\frac{E_d}{RT} + \ln(\nu) \qquad \text{(S3)}$$

Table S3: Fitting results ($y = a + bx$) as well as desorption energies and prefactors for the mLEA of PEN and PFP on MoS_2 as shown in Figure S3.

Coverage [ML]	***a***	***b* [K]**	**E_d [kJ/mol]**	**ν [s^{-1}]**
PEN				
0.17	25.6±0.7	-13172±304	109.5±2.5	$10^{11.1\pm0.3}$
0.42	25.6±0.6	-13015±261	108.2±2.2	$10^{11.1\pm0.3}$
0.72	25.5±1.2	-12638±478	105.1±4.0	$10^{11.1\pm0.5}$
1.00	32.7±1.9	-15319±747	127.4±6.2	$10^{14.2\pm0.8}$
1.19	33.1±1.7	-14767±611	122.8±5.1	$10^{14.4\pm0.7}$
PFP				
0.15	28.9±1.7	-15921±801	132.4±6.7	$10^{12.6\pm0.7}$
0.44	27.6±2.1	-14905±916	123.9±7.6	$10^{12.0\pm0.9}$
0.69	28.2±2.4	-14604±1000	121.4±8.3	$10^{12.3\pm1.0}$
1.00	32.3±1.8	-15553±717	129.3±6.0	$10^{14.0\pm0.8}$
1.04	32.0±5.1	-14947±1900	124.3±15.8	$10^{13.9\pm2.2}$

5. Heating rate variation data and analysis

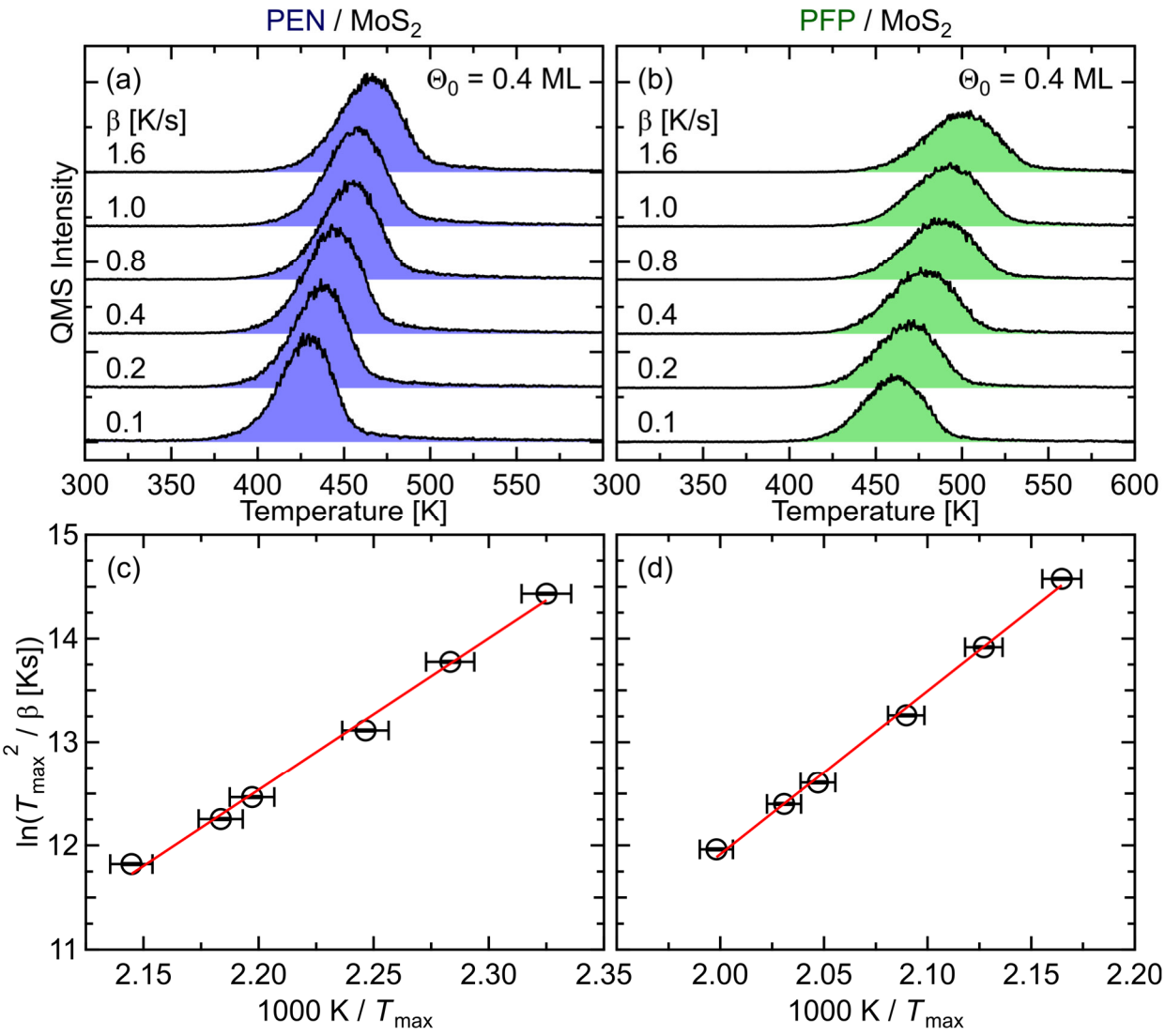

Figure S4: (a) and (b) Heating-rate variation (HRV) series for PEN and PFP, respectively, on MoS_2 for heating rates from 0.1 to 1.6 K/s. Initial coverages were prepared by depositing 8 Å of the molecules and annealing the sample to 430 K and 455 K for 10 s for PEN and PFP, respectively, yielding coverages of 0.4 ML for both molecules. (c) and (d) Linear fit (red line) of $\ln(T_{max}^2/\beta)$ vs. $1/T_{max}$. The fitting results are given in Table S4. The error bars in (c) and (d) are based on an error of ± 2 K for the temperature of the desorption maximum, T_{max}.

Heating-rate variation (mLEA) analysis, according to:

$$\ln\left(\frac{T_{max}^2}{\beta}\right) = \frac{E_d}{RT_{max}} + \ln\left(\frac{E_d}{R\nu}\right) \qquad \text{(S4)}$$

Table S4: Fitting results of ($y = a + bx$) as well as desorption energies and prefactors for the HRV analysis of PEN and PFP on MoS_2 as shown in Figure S4.

Coverage [ML]	***a***	***b* [K]**	E_d **[kJ/mol]**	**ν [s^{-1}]**
PEN				
0.4	-19.7±1.2	14665±538	121.9±4.5	$10^{12.7\pm0.5}$
PFP				
0.4	-19.6±1.0	15760±471	131.0±3.9	$10^{12.7\pm0.4}$

Table S5: Fitting results of ($y = a + bx$) as well as desorption energies and prefactors for the HRV analysis of PEN and PFP on MoS_2 considering a 2 K higher T_{max}.

Coverage [ML]	***a***	***b* [K]**	E_d **[kJ/mol]**	**ν [s^{-1}]**
PEN				
0.4	-19.9±1.2	14801±544	123.1±4.5	$10^{12.8\pm0.5}$
PFP				
0.4	-19.7±1.0	15896±476	132.2±4.0	$10^{12.8\pm0.4}$

Table S6: Fitting results of ($y = a + bx$) as well as desorption energies and prefactors for the HRV analysis of PEN and PFP on MoS_2 considering a 2 K lower T_{max}.

Coverage [ML]	***a***	***b* [K]**	E_d **[kJ/mol]**	**ν [s^{-1}]**
PEN				
0.4	-19.6±1.2	14531±533	120.8±4.4	$10^{12.7\pm0.5}$
PFP				
0.4	-19.5±1.0	15625±467	129.9±3.9	$10^{12.6\pm0.4}$

As can be seen in Figures S4 (c),(d), the error introduced by a desorption temperature error ΔT_{max} of ±2 K yields very small error bars along the vertical axis and larger error bars along the horizontal axis. All data points lie on the linear fit line if the margin of error is considered. Furthermore, the deviations in the desorption energy resulting from ΔT_{max} is ± 1.1 kJ/mol for both systems, which is smaller than the fitting error.

6. Derivation of the Gibbs free energy difference upon desorption of molecular mono- and multilayers

In transition state theory (TST), the rate constant, k_{TST}, can be expressed as a function of the standard Gibbs free energy of activation, $\Delta G^{\ddagger}$:

$$k_{\mathrm{TST}} = \frac{k_{\mathrm{B}}T}{h} \exp\left(-\frac{\Delta G^{\ddagger}}{RT}\right), \tag{S5}$$

where k_{B} is Boltzmann's constant, T is the temperature, h is Planck's constant, and R is the universal gas constant. In the here considered case of thermal desorption, $\Delta G^{\ddagger}$ describes the change of the standard Gibbs free energy upon transition from the adsorbed state to the transition state of desorption. $\Delta G^{\ddagger}$ is related to the standard enthalpy of activation, $\Delta H^{\ddagger}$, and the standard entropy of activation, $\Delta S^{\ddagger}$, of the desorption process by equation S6:

$$\Delta G^{\ddagger} = \Delta H^{\ddagger} - T\Delta S^{\ddagger} \tag{S6}$$

Inserting equation S6 into equation S5 leads to equation S7, which shows the entropic and enthalpic contributions to k_{TST} as separate terms:

$$k_{\mathrm{TST}} = \frac{k_{\mathrm{B}}T}{h} \exp\left(\frac{\Delta S^{\ddagger}}{R}\right) \exp\left(-\frac{\Delta H^{\ddagger}}{RT}\right). \tag{S7}$$

The activation energy of desorption, or desorption energy E_{d}, is defined by the empirical Arrhenius equation for the rate constant k_{A}:

$$k_{\mathrm{A}} = \nu \exp\left(-\frac{E_{\mathrm{d}}}{RT}\right). \tag{S8}$$

After taking the logarithm, equation S8 can be re-written in differential form:

$$E_{\mathrm{d}} = -R\frac{\mathrm{d}\ln k_{\mathrm{A}}}{\mathrm{d}\left(\frac{1}{T}\right)}. \tag{S9}$$

Likewise, equation S7 can be logarithmized and re-written in differential form:

$$\Delta H^{\ddagger} = -R\frac{\mathrm{d}\ln\left(\frac{k_{\mathrm{TST}}}{T}\right)}{\mathrm{d}\left(\frac{1}{T}\right)}. \tag{S10}$$

Here, we have assumed that $\Delta H^{\ddagger}$ and $\Delta S^{\ddagger}$ are independent of the temperature. To establish a relationship between E_{d} with $\Delta H^{\ddagger}$, we subtract equation S10 from equation S9:

$$E_{\mathrm{d}} - \Delta H^{\ddagger} = -R\left[\frac{\mathrm{d}\ln k_{\mathrm{A}}}{\mathrm{d}\left(\frac{1}{T}\right)} - \frac{\mathrm{d}\ln\left(\frac{k_{\mathrm{TST}}}{T}\right)}{\mathrm{d}\left(\frac{1}{T}\right)}\right]$$

$$= -R\frac{(\mathrm{d}\ln k_{\mathrm{A}} - \mathrm{d}\ln k_{\mathrm{TST}}) - \mathrm{d}\ln\left(\frac{1}{T}\right)}{\mathrm{d}\left(\frac{1}{T}\right)}. \tag{S11}$$

Assuming that $k_{\mathrm{TST}} = k_{\mathrm{A}}$, we obtain:

$$E_{\mathrm{d}} - \Delta H^{\ddagger} = R \frac{\mathrm{d} \ln\left(\frac{1}{T}\right)}{\mathrm{d}\left(\frac{1}{T}\right)} = RT. \tag{S12}$$

Replacing $\Delta H^{\ddagger}$ in equation S7 with equation S12 leads to:

$$k_{\mathrm{TST}} = \frac{k_{\mathrm{B}} T}{h} \exp\left(\frac{\Delta S^{\ddagger}}{R} + 1\right) \exp\left(-\frac{E_d}{RT}\right). \tag{S13}$$

Comparing equation S13 to the Arrhenius equation (equation S8) and again assuming that $k_{\mathrm{TST}} = k_{\mathrm{A}}$, we can express the prefactor ν in the Arrhenius equation in terms of TST:

$$\nu = \frac{k_{\mathrm{B}} T}{h} \exp\left(\frac{\Delta S^{\ddagger}}{R} + 1\right). \tag{S14}$$

Now, using equation S14, differences in the entropy gain upon desorption from different adsorbed phases, e.g., mono- and multilayers, can be calculated from the respective prefactors:

$$\Delta S^{\ddagger}{}_{\mathrm{multi}} - \Delta S^{\ddagger}{}_{\mathrm{mono}} = R \ln\left(\frac{\nu_{\mathrm{multi}}}{\nu_{\mathrm{mono}}}\right). \tag{S15}$$

Inserting equations S12 and S15 into equation S6, we obtain equation (5) in the main text.

7. Estimation of energy of attractive intermolecular interactions required to overcome entropic stabilization

According to equation (5), the first molecular layer is more stable than subsequent layers if

$$\Delta G^{\ddagger}_{\text{mono}} - \Delta G^{\ddagger}_{\text{multi}} > 0. \qquad \text{(S16)}$$

If we assume that, due to the attractive intermolecular interactions, molecules form islands even in the zero-coverage limit, meaning that attractive interactions are always constant, we can add an energy E_{attr} to the desorption energies in the zero-coverage limit in equation (5) in the main text and obtain

$$\Delta G^{\ddagger}_{\text{mono}} - \Delta G^{\ddagger}_{\text{multi}} = (E_{d,\,\text{mono}} + E_{\text{attr}}) - E_{d,\,\text{multi}} + RT \ln\left(\frac{\nu_{\text{multi}}}{\nu_{\text{mono}}}\right) > 0 \qquad \text{(S17)}$$

and thus

$$E_{\text{attr}} > E_{d,\,\text{multi}} - E_{d,\,\text{mono}} - RT \ln\left(\frac{\nu_{\text{multi}}}{\nu_{\text{mono}}}\right). \qquad \text{(S18)}$$

as a condition for a stabilization of a first molecular layer that forms crystalline islands. If we assume no entropic stabilization, the prefactor of monolayer desorption must be equal to or larger than that of the multilayers, $\nu_{\text{mono}} \geq \nu_{\text{multi}}$. With this restriction, the term $\ln\left(\nu_{\text{multi}}/\nu_{\text{mono}}\right)$ is minimum for equal prefactor for mono- and multilayer desorption. Thus, the minimum energy of attractive intermolecular interactions to stabilize the first molecular layer is given by the zero-coverage desorption energies of mono- and multilayer:

$$E^{\text{min}}_{\text{attr}} > E_{d,\,\text{multi}} - E_{d,\,\text{mono}}\,. \qquad \text{(S19)}$$

For PEN and PFP, this equation yields values of (19 ± 6) kJ/mol and (18 ± 5) kJ/mol, respectively, which yields a weighted average of (18 ± 4) kJ/mol. If we assume a larger prefactor for monolayer desorption, as for instance observed for PEN on Au(111) with $\nu \sim 10^{19}$ s^{-1}, [S11] these energies increase by approximately 20 kJ/mol.

Note that these energies are the total energy required to act on a single molecule from attractive intermolecular interactions with its surroundings, not attractive energies from pair-wise molecular interactions.

8. Fits of the Polanyi-Wigner equation to the monolayer TPD traces

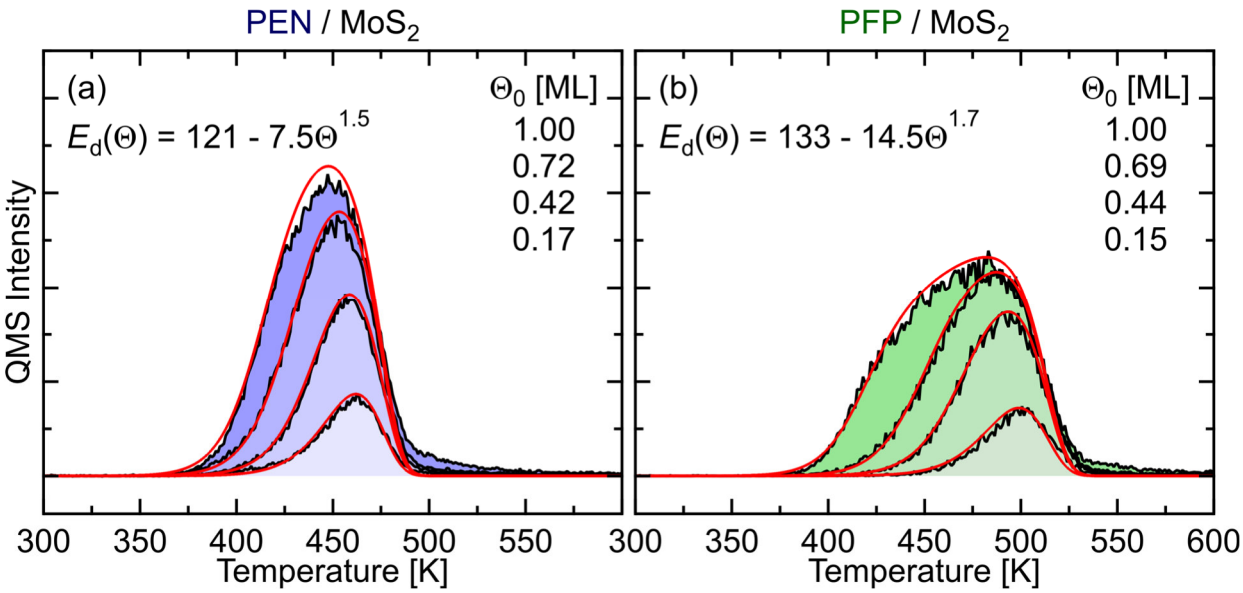

Figure S5: (a) and (b) TPD coverage series of PEN and PFP on MoS2 (black lines) and simulated TPD traces (red lines) using an exponential function for the desorption energy (shown in graphs, in kJ/mol). Constant prefactors, as obtained by the MC simulations, were used (PEN: $10^{12.5}$ s^{-1}, PFP: $10^{12.7}$ s^{-1}).

The simulations of TPD traces were performed according to equation S20:

$$r = \nu\, \Theta \exp\left(-\frac{E_d - a\theta^b}{RT}\right) \qquad \text{(S20)}$$

9. Analysis of the STM data of the mixed PEN + PFP film on MoS_2

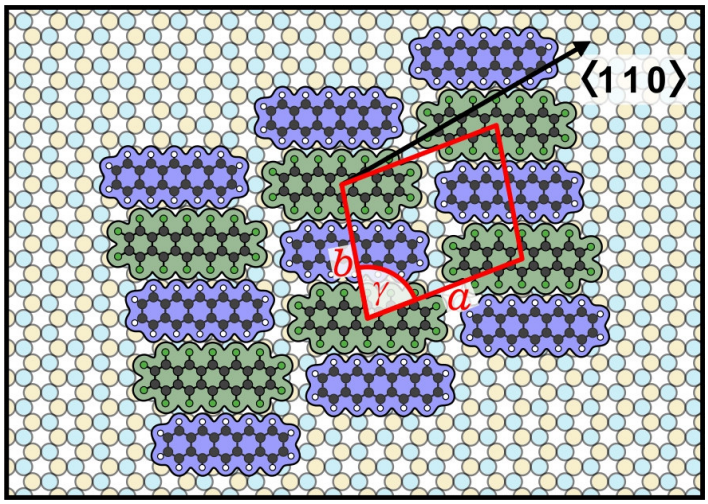

Figure S6: Illustration of the structural model for the stoichiometric 1:1 intermixture of PEN and PFP on MoS_2 based on STM results.

From the STM micrograph in Figure 4, we find an oblique unit cell with a = (16.2 ± 1.0) Å, b = (14.6 ± 1.0) Å and γ = (83 ± 5)°. The angle between the long side of the unit cell and the $\langle 110 \rangle_{MoS_2}$ azimuth (determined from LEED data of the MoS_2 crystal) is (3 ± 5)°. The angle between the long molecular axes and the $\langle 110 \rangle_{MoS_2}$ azimuth is (35 ± 5)°.

The experimentally determined unit cell parameters are in good agreement with a $\begin{pmatrix} 5 & 1 \\ -4 & 5 \end{pmatrix}$ commensurate superstructure that is illustrated in Figure S6. The corresponding unit cell parameters are a = 17.4 Å, b = 14.5 Å and γ = 80°. The angle between long side of the unit cell and the $\langle 110 \rangle_{MoS_2}$ azimuth is 9°. The angle between the long molecular axes and the $\langle 110 \rangle_{MoS_2}$ azimuth is 30°.

10. References

[S1] Meng, B.; Weinberg, W. H. Monte Carlo Simulations of temperature programmed desorption spectra. *J. Chem. Phys.* **1994**, 100, 5280-5289.

[S2] Jin, C.; Rasmussen, F. A.; Thygesen, K. S. Tuning the Schottky Barrier at the Graphene/MoS_2 Interface by Electron Doping: Density Functional Theory and Many-Body Calculations. *J. Phys. Chem. C* **2015**, 119, 19928-19933.

[S3] Shen, N.; Tao, G. Charge Transfer and Interface Engineering of the Pentacene and MoS_2 Monolayer Complex. *Adv. Mater. Interfaces* **2017**, 4, 1601083.

[S4] Klues, M.; Witte, G. Crystalline packing in pentacene-like organic semiconductors. *CrystEngComm* **2018**, 20, 63-74.

[S5] Allinger, N. L.; Yuh, Y. H.; Lii, J.-H. Molecular Mechanics. The MM3 Force Field for Hydrocarbons. 1. *J. Am. Chem. Soc.* **1989**, 111, 8551-8561.

[S6] Allinger, N. L.; Zhou, X.; Bergsma, J. Molecular mechanics parameters. *J. Mol. Struc.* **1994**, 312, 69-83.

[S7] Widdascheck, F.; Hauke, A. A.; Witte, G. A Solvent-Free Solution: Vacuum-Deposited Organic Monolayers Modify Work Functions of Noble Metal Electrodes. *Adv. Funct. Mater.* **2019**, 1808385.

[S8] Lin, J.; Zhong, J.; Zhong, S.; Li, H.; Zhang, H.; Chen, W. Modulating electronic transport properties of MoS_2 field effect transistors by surface overlayers. *Appl. Phys. Lett.* **2013**, 103, 063109.

[S9] Ning-Tong, C.; Lei, Z.; Lu, L.; Hai-Peng, X.; Han, H.; Dong-Mei, N.; Yong-Li, G. The van der Waals heterostructures of CuPc/MoS_2(0001). *Acta Phys. Sin.* **2014**, 63, 167903.

[S10] Lee, S. Y.; Kim, U. J.; Chung, J.; Nam, H.; Jeong, H. Y.; Han, G. H.; Kim, H.; Oh, H. M.; Lee, H.; Kim, H.; Roh, Y.-G.; Kim, J.; Hwang, S. W., Park, Y.; Lee, Y. H. Large Work Function Modulation of Monolayer MoS_2 by Ambient Gases. *ACS Nano* **2016**, 10, 6100-6107.

[S11] Käfer, D.; Wöll, C.; Witte, G. Thermally activated dewetting of organic thin films: the case of pentacene on SiO_2 and gold. *Appl. Phys. A* **2009**, 95, 273-284.